Magnon superlattices around skyrmions in frustrated magnets

Adarsh Hullahalli [1,2] Christos Panagopoulos [1] and Christina Psaroudaki [2,*]

[1]*Division of Physics and Applied Physics, School of Physical and Mathematical Sciences, Nanyang Technological University, 637371 Singapore, Singapore*

[2]*Laboratoire de Physique de l'École Normale Supérieure, ENS, Université PSL, CNRS, Sorbonne Université, Université de Paris, F-75005 Paris, France*

(Received 12 August 2025; accepted 19 September 2026; published 2 November 2026)

Dynamic magnetic textures provide a versatile platform for controlling magnon states in spintronic systems. Here, we identify a class of crystal-like dynamical magnon patterns in centrosymmetric frustrated magnets. Their periodicity originates from the interference of symmetry-related finite-wave-vector magnons associated with the Mexican-hat dispersion of the uniformly magnetized state. In the presence of an atomic-scale skyrmion whose size is comparable to the low-energy magnon wavelength, these extended states hybridize with magnetically active skyrmion modes. The skyrmion breaks translational symmetry, selects a coherent finite-k superposition, and allows the resulting magnon superlattice to be efficiently excited by a spatially uniform ac field. A local Gaussian ac field generates the same pattern without a skyrmion, showing that the skyrmion selects and activates, rather than sets, the superlattice wavelength. In addition, helicity dynamics enables weak activation of otherwise magnetically inactive breathing modes, while skyrmion lattices support dispersive magnon bands with nontrivial Chern numbers inside the first magnon gap. These results establish frustrated magnets as a platform for controllable finite-wavelength magnon interference and texture-assisted spin-wave patterning.

DOI: 10.1103/fhbj-ykvn

I. INTRODUCTION

The interaction of multiple length scales can give rise to hybridization effects and emergent phenomena that transcend the properties of individual constituents. When characteristic lengths, such as domain sizes, coherence lengths, or moiré pattern periodicities, become comparable, superlattice structures with fundamentally new functionalities emerge. This convergence of scales enables the design and control of complex quantum states, including unconventional superconductivity and topologically nontrivial phases, opening pathways toward materials with tailored electronic, magnetic, and optical properties [1–5].

Competing magnetic interactions and length scales can give rise to new states of matter. Magnetic skyrmions, topologically protected spin textures, have emerged as a key example due to their potential applications in spintronics and quantum computing [6,7]. Although skyrmions are commonly found in noncentrosymmetric materials with strong Dzyaloshinskii-Moriya interactions (DMIs), they can also form in centrosymmetric frustrated magnets due to competing exchange interactions [8]. Unlike DMI-based skyrmions, which arise from broken inversion symmetry and exhibit fixed chirality, frustrated magnets allow for smaller and chirality-flexible structures [9]. This inherent ground-state degeneracy makes them a unique platform for exploring exotic spin patterns and quantum effects [10,11].

Understanding the magnon spectrum, the collective spin-wave excitations, around skyrmions is essential for understanding their fundamental physics and assessing their potential for information storage and processing [12]. These excitations play a key role in skyrmion stability and provide a means to manipulate skyrmion motion and interactions through external stimuli [13–15]. The magnon spectrum around a skyrmion can exhibit distinct features such as chiral edge modes [16] and finely spaced emergent Landau levels [17]. The interplay between magnons and skyrmions can lead to emergent phenomena, including nonreciprocal behavior and long-range propagation characteristics [18]. Understanding these features has driven exciting advances in experimental techniques for probing spin-wave excitations, such as inelastic neutron scattering [19], Brillouin light scattering [20], and ferromagnetic (FM) resonance [21,22].

Collective spin excitations in frustrated magnets differ from those in DMI-based systems due to the unique properties of their skyrmions. The additional helicity degree of freedom couples to magnon modes, enabling rich hybridization dynamics. Because skyrmions in frustrated magnets are typically smaller, the number of internal deformation modes they can support is limited. The skyrmion core induces spatially modulated fluctuations in its vicinity that mediate long-range interactions and reshape the magnon propagation landscape.

We begin by studying the magnon spectrum around an isolated skyrmion and a skyrmion lattice. The small size of

*Contact author: christina.psaroudaki@phys.ens.psl.fr

Published by the American Physical Society under the terms of the Creative Commons Attribution 4.0 International license. Further distribution of this work must maintain attribution to the author(s) and the published article's title, journal citation, and DOI.

frustrated skyrmions confines localized deformation modes to the magnon continuum, where they hybridize with extended states. A novel magnon superlattice pattern arises from interference between finite-wave-vector magnon modes associated with the characteristic Mexican-hat dispersion. In the presence of a skyrmion, coupling to its magnetically active modes selects a coherent interference pattern from the extended magnon continuum and gives it a uniform magnetic dipole moment, making it accessible to spatially uniform ac drives. The same pattern can also be generated in the absence of a skyrmion by a local ac field whose width is comparable to the low-energy magnon wavelength. Spin-wave interference underlies several proposals and demonstrations of reconfigurable magnonic functionality, including majority gates [23], magnon transistors [24], directional couplers [25], and wavelength-controlled interferometers [26]. In this broader context, our results reveal a new route to controlled magnon interference, where a skyrmion selects and activates finite-wavelength magnon patterns. This establishes a paradigm of emergent confinement in magnonic systems and provides insight into how topological textures shape quasiparticle interference in quantum materials.

While the system hosts several counterclockwise (CCW) modes, it lacks magnetically active breathing modes due to its S_z-conserving $U(1)$ symmetry. Because the Hamiltonian is invariant under global rotations around the z axis, the longitudinal spin is conserved within linear order. The breathing modes have a vanishing magnetic dipole moment and cannot be excited directly by a uniform out-of-plane ac field. They can, however, be weakly activated through damping-mediated coupling to the driven helicity dynamics. Magnon excitations in frustrated magnets hybridize with the helicity-zero mode, particularly in breathing modes, leading to helicity precession. Bands in skyrmion lattices exhibit complex k dependence and are characterized by finite Chern numbers within the first magnon gap, with a sign that depends on skyrmion charge. In systems of interacting skyrmions, emergent low-energy modes are characterized by complex dynamics related to the precession of skyrmion helicity.

II. MODEL AND METHODS

We consider classical spins, $\mathbf{S}_i$, defined on a two-dimensional (2D) x–y lattice with FM nearest-neighbor and competing skyrmion-stabilizing spin interactions $E_{\rm SM}$,

$$H = -J_1 \sum_{\langle i,j\rangle} \mathbf{S_i}\cdot\mathbf{S_j} + E_{\rm SM} - h\sum_i S_i^z - K\sum_i (S_i^z)^2, \quad (1)$$

where $\langle i, j\rangle$ sums over nearest-neighbor pairs, while the third and fourth terms represent the interaction with the magnetic field aligned along the z axis and the single-ion magnetic anisotropy, respectively. Here, we focus on the magnetization dynamics in the presence of competing antiferromagnetic interactions on a triangular lattice of the form $E_{\rm SM} = E_{\rm FM} = J_2\sum_{\langle\langle i,j\rangle\rangle}\mathbf{S_i}\cdot\mathbf{S_j}$, where $\langle\langle i, j\rangle\rangle$ denote pairs of next-nearest-neighbor pairs. When necessary, we compute the magnon spectrum in chiral skyrmions with DMI, $E_{\rm SM} = E_{\rm DMI} = \sum_{\langle i,j\rangle}\mathbf{D}_{ij}\cdot\mathbf{S_i}\times\mathbf{S_j}$, to facilitate comparison and highlight the distinct nature of magnons in frustrated magnets.

The zero-temperature phase diagram of the model (1) as a function of h and K includes eight distinct phases, comprising a skyrmion crystal and a fully polarized FM state [8,27]. In the continuum limit, $\mathbf{m}_i = \mathbf{S}_i/S$, with S the total spin, becomes a field $\mathbf{m}(r)$, typically expressed in spherical coordinates as $\mathbf{m} = [\sin\Theta\cos\Phi, \sin\Theta\sin\Phi, \cos\Theta]$. Isolated skyrmions appear as metastable defects above the FM state, described by $\Phi = \mu\phi + \varphi_0$ and $\Theta(\mathbf{r}) = \Theta(\rho)$, in polar coordinates $\mathbf{r} = (\rho, \phi)$, where φ_0 is the helicity and μ the vorticity. These topological solutions have integer charge $Q = \int d\mathbf{r}\ \mathbf{m}\cdot(\partial_x\mathbf{m}\times\partial_y\mathbf{m})/(4\pi) = -\mu$, assuming an FM background $\mathbf{m}_{\rm FM} = (0, 0, 1)$. Since the energy is independent of φ_0 and the sign of μ, skyrmions ($\mu = 1$, $Q = -1$) and antiskyrmions ($\mu = -1$, $Q = 1$) have the same energy, and the helicity is a zero mode.

The energy in Eq. (1) is minimized using an iterative simulated annealing procedure combined with single-step Monte Carlo dynamics based on the Metropolis algorithm [28]. Magnon modes are calculated around a stable classical state using linear spin-wave theory by applying the Holstein-Primakoff transformation [29] and an expansion in powers of $1/S$. The details of calculating and diagonalizing the spin-wave Hamiltonian $H_{\rm SW}$ [30,31] are reviewed in Appendix A of the Supplemental Material (SM) [32]. Simulations were conducted with periodic boundary conditions on triangular lattices of size 42×42, unless stated otherwise. The magnetization dynamics are obtained by numerically solving the Landau-Lifshitz-Gilbert (LLG) equation [33] using the fourth-order Runge-Kutta method and a Gilbert damping parameter $\alpha = 0.01$.

For clarity, we briefly summarize the quantities used throughout the work. The dynamic magnetic dipole moment $\mathbf{M}$ characterizes the coupling strength of each magnon mode to a spatially uniform oscillating magnetic field and identifies modes that are active under uniform driving. Modes with vanishing $\mathbf{M}$ may nevertheless couple to a spatially nonuniform field through the overlap of their local magnetic-moment density with the field profile. The spatial deformation of a mode is visualized by $\Delta\mathbf{S_n}$, which represents the real-space spin deviation in the coherent magnon representation relative to the static skyrmion background. The quantity $\mathcal{D}S(t)$ denotes the time-dependent deviation of the spin field obtained from micromagnetic simulations under an ac drive, while ϕ_0 refers to the helicity angle of a skyrmion—the global rotation of in-plane spins around the z axis—and φ defines the relative helicity between two skyrmions.

III. MAGNON SUPERLATTICES

A. Skyrmion-enabled magnon superlattice modes

We first consider the case of an isolated skyrmion, a metastable state within the uniformly magnetized phase for fields above the critical value $h_c = J_2 - 2K$, with its spin configuration shown in Fig. 1(a). The skyrmion profile $\theta_i = \arccos S_i^z$ depicted in Fig. 1(b) (red solid line) exhibits oscillations and decays away from the skyrmion core [8,9]. Therefore, the skyrmion tail can be regarded as an excitation in the FM state, induced by the nonlinear core and extending into the topologically trivial region surrounding the skyrmion.

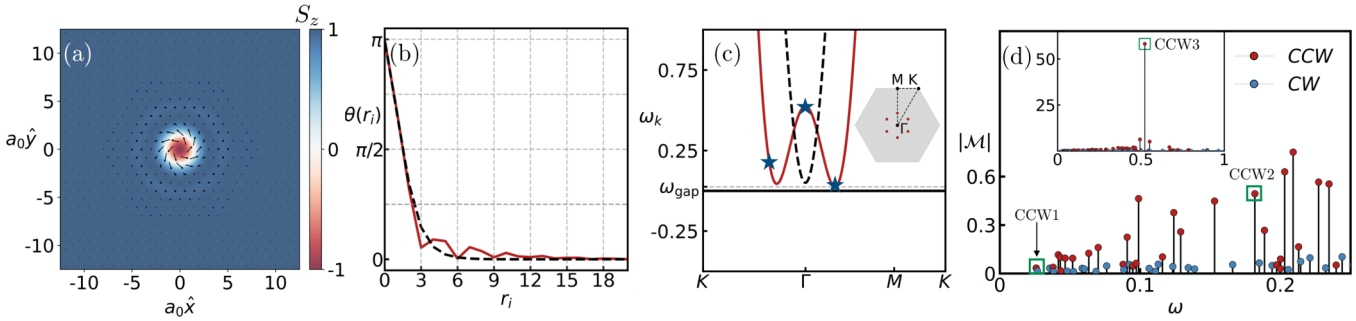


FIG. 1. Finite-wavelength magnon excitations matching skyrmion size. (a) Isolated skyrmion of a frustrated magnet in a triangular lattice with $J_1 = 1$, $J_2 = 0.5$, $h = 0.225/S$, and $K = 0.15$. (b) Skyrmion profile calculated along a line passing through the skyrmion center as $\theta(r_i) = \arccos S_i^z$ for isolated skyrmions in frustrated (red line) and chiral magnets (black line), which illustrates the skyrmion tails, unique to frustrated magnets. (c) Low-energy dispersion of magnon excitations around the uniformly magnetized state of a frustrated (red line) and chiral magnet (black line) along the Γ-*M*-*K* direction. The Mexican hatlike shape in frustrated magnets introduces complexity to the magnon dynamics around skyrmions. (d) Magnetic dipole moment $|\mathcal{M}|$ of the magnon modes around a single skyrmion.

For the parameters considered, the skyrmion core diameter is $\lambda = 12a$, with a the lattice constant, determined from the points where θ_i vanishes, and it depends only weakly on the applied magnetic field. The oscillatory tail is a known consequence of the finite-wave-vector response of frustrated magnets with competing exchange interactions [8,9], and is absent in DMI skyrmions, with an exponentially decaying skyrmion profile shown in Fig. 1(b) (black dashed line).

For the parameters considered, the characteristic skyrmion diameter is $\lambda \simeq 12a$, defined from the radial distance over which $\theta(r)$ falls below our numerical resolution. The skyrmion texture has an energy equal to $\Delta E_{\rm Sk} = E_{\rm Sk} - E_{\rm FM} = 0.22J_1$. Small-amplitude spin waves in the FM state appear as traveling waves with a dispersion $\omega_{\mathbf{k}}$ depicted in Fig. 1(c). The energy-momentum cut along the high-symmetry Γ-*M*-*K* direction exhibits a Mexican hatlike shape [34,35]. Along this path, the low-energy magnon dispersion features one gapped minimum, $k^1_{\rm min}$, marked by red dots in the hexagonal Brillouin zone, with a gap given by $\omega_{\rm gap} = h + 2K - J_2$. In total, there are six degenerate minima, corresponding to spin waves with wave vectors matching the characteristic length scale of the model (1) and propagating along the lattice vectors of the 2D triangular lattice. These finite-k magnons are generic consequences of the Mexican-hat dispersion of frustrated ferromagnets and are not specific to skyrmions. In contrast, spin waves in DMI systems propagate with a quadratic dispersion $\omega_k \propto k^2$ above the magnon gap, shown in Fig. 1(c) with a black dashed line. The plotted curve shows the symmetric branch $\omega_{|k|}$; thus, the dispersion shift at a finite k_D caused by the DMI term [36] is not visible as the opposite $\pm k$ contributions overlap. Similar to other topological objects [37,38], the presence of a skyrmion creates a confining potential for magnons, giving rise to localized modes that correspond to deformations. In chiral magnets, the wavelength of the low-energy magnon continuum is considerably larger than the skyrmion size ($l_{\rm min} = 2\pi/k_{\rm min} \gg \lambda$), such that the skyrmion barely perturbs the extended magnon modes [38]. In frustrated magnets, however, the situation is qualitatively different. Here, the low-energy magnons have a finite wavelength comparable to the skyrmion size, $l_{\rm min} \sim \lambda$, enabling strong coupling between the two. Since the skyrmion size is small, it supports no internal excitations below $\omega_{\rm gap}$. We find several deformation-related states that lie within the magnon continuum and are hybridized with extended modes.

We now analyze the magnon modes, concentrating on those that are magnetically active, characterized by a finite magnetic dipole moment $\boldsymbol{\mathcal{M}}_\mu$ [39], with $\mu = \{x, y, z\}$. In chiral skyrmions, magnetic resonance studies investigating the response to a uniform oscillatory magnetic field have identified three characteristic in-gap magnon modes: a clockwise (CW) and CCW gyration of the skyrmion core, associated with a finite $\mathcal{M}_{x,y}$ induced by in-plane ac fields, and a breathing mode with a finite $\mathcal{M}_z$ that emerges under longitudinal ac fields [12,40,41]. The CW and CCW labels are assigned from the relative phase of the complex in-plane magnetic dipole components $\mathcal{M}_y/\mathcal{M}_x = \pm i$ and correspond to opposite senses of circular precession, with the convention fixed by the time dependence $e^{-i\omega t}$. Antiskyrmion resonances are found at the same frequencies as skyrmion modes, but with opposite sense of gyration (CCW skyrmion modes correspond to CW antiskyrmion modes and vice versa) [42]. We therefore focus on skyrmions with $Q = -1$ and omit the discussion of antiskyrmions with $Q = 1$.

Above the magnon gap, we identify the CCW, CW, breathing, and multipolar modes as hybridized excitations of the skyrmion and the surrounding FM region. As a result, these modes are influenced by the distinctive dispersion of the uniformly magnetized state [see Fig. 1(c)]. For the parameters considered here, we focus on the CCW modes that carry substantially larger in-plane magnetic dipole moments than their CW counterparts and will dominate the driven response. The lowest mode near $\omega_{\rm gap}$ is a CCW mode with a finite $\mathcal{M}_x$ [CCW1 mode in Fig. 1(d)]. Figure 2 illustrates the real-space deformation ΔS_z [panel (a)] and ΔS_x [panel (b)] defined as $\Delta \mathbf{S}_{\mathbf{n},i} = \langle \mathbf{S}_{\mathbf{n},i} \rangle - S\mathbf{v}_i^3$, with $\mathbf{v}_i^3$ a vector aligned with the classical skyrmion state $\mathbf{S}_{i,0}$. $\langle \mathbf{S}_{\mathbf{n},i} \rangle$ is over the coherent magnon representation [16,43] (see Appendix B of SM [32] for definitions). Notably, ΔS_x exhibits a crystal-like structure away from the skyrmion core, which arises due to interference effects between the six degenerate extended states with $k^i_{\rm min}$, with $i = \{1, 6\}$, that exist at the same energy [see Fig. 1(c)]. The crystal-like structures correspond to localization patterns

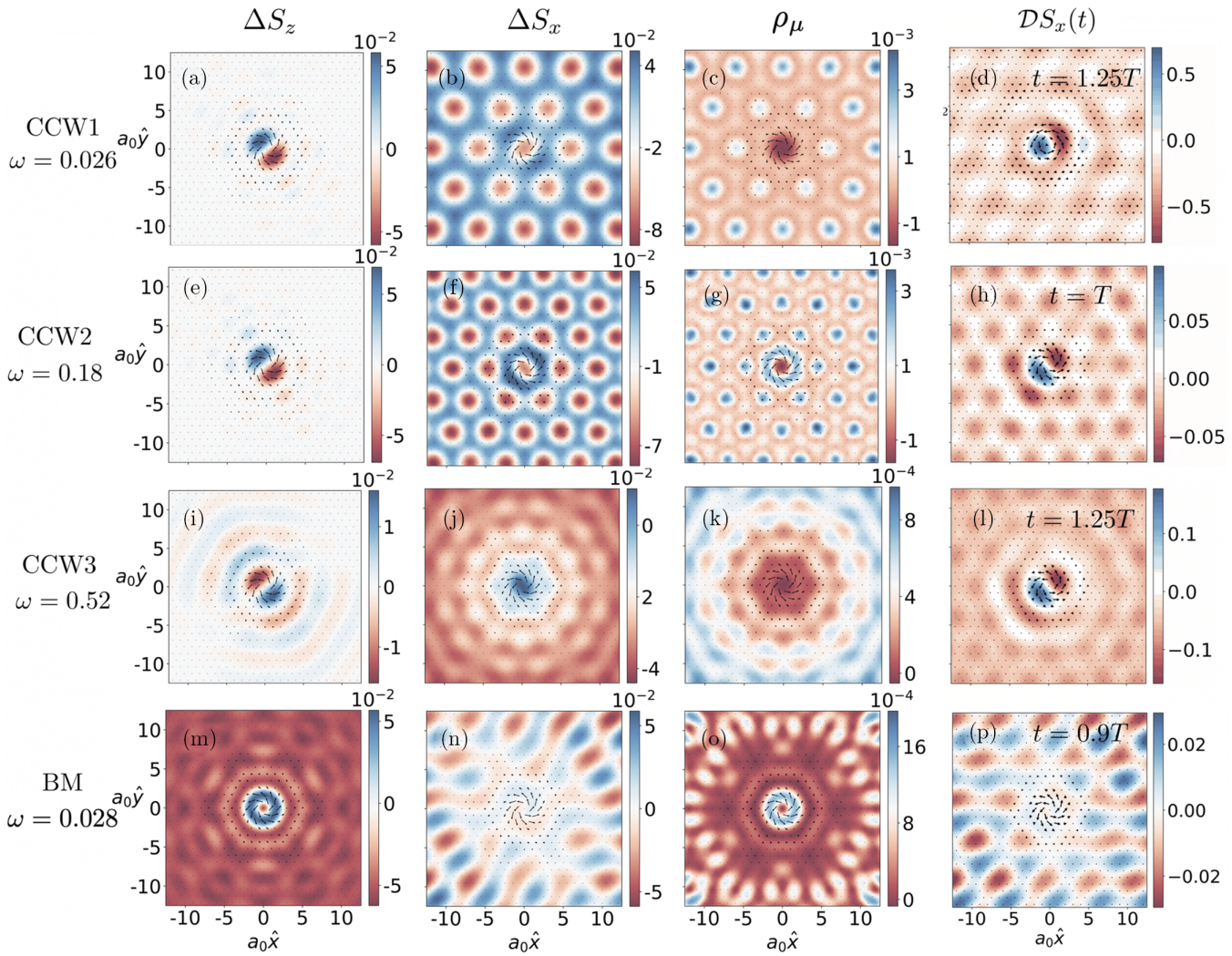


FIG. 2. Observable magnon superlattices. Crystal-like localization patterns of magnon modes in the presence of a skyrmion. (a)–(d) Real-space deformation ΔS_z and ΔS_x, local bosonic BdG weight ρ_μ, and real-time dynamics $\mathcal{D}S_x(t)$ for the low-lying CCW1 hybridized with interference patterns of finite-wavelength extended states. (e)–(h) Same quantities for the CCW2 mode, exhibiting magnon crystals with shorter periodicity. (i)–(k) The symmetric localization patterns of the high in energy CCW3 mode with the largest $\mathcal{M}_x$. (m)–(p) The lowest-lying breathing mode has a vanishing $\mathcal{M}_z$, but is weakly activated through damping-mediated coupling to the driven helicity dynamics. Here, we use the parameters of Fig. 1.

of the local bosonic BdG weight ρ_{CCW1}, shown in Fig. 2(c). These localization patterns correspond to the spatial concentration of magnon intensity into interference maxima.

These interference patterns emerge from the wavelike behavior of magnons. To isolate the role of the frustrated-magnet dispersion, we compare with the reference state $|\Psi\rangle = \sum_{i=1}^{6} |\mathbf{k}_{\mathrm{min}}^{i}\rangle$ plotted in Fig. S1 in the SM [32] in the coherent-state representation. This constructed equal-phase superposition has no uniform magnetic dipole moment and therefore cannot be excited by a spatially uniform ac magnetic field. It produces, however, a crystal-like pattern with the same periodicity, showing that the Mexican-hat magnon dispersion sets the length scale of the superlattice. The skyrmion breaks translational symmetry, mixes the degenerate finite-k_{min} states, fixes their relative phases, and transfers uniform magnetic dipole weight to the resulting hybridized CCW mode. A local ac field whose width is comparable to the low-energy magnon wavelength can also break translational symmetry and excite the same characteristic pattern in the absence of a skyrmion, as shown in Fig. S8 in Appendix F of the SM [32]. The skyrmion therefore acts as an intrinsic nanoscale mode-selecting element that makes the interference state accessible to a spatially uniform drive. This coherent mixing of extended states with different momenta manifests as spatially modulated localization superlattices, with an amplitude that survives far away from the skyrmion core [see Fig. S1(b) in the SM [32]]. Such skyrmion-hybridized patterns are a hallmark of strong magnon-skyrmion coupling in frustrated systems and are absent in the conventional chiral-magnet comparison, where the mismatch in length scales suppresses the finite-wavelength interference mechanism.

To investigate whether this novel magnon mode localization pattern leads to observable patterns, we numerically solve the LLG equation [33] for magnetization dynamics under $\mathbf{H}_{\mathrm{ac}} = h_{\mathrm{ac}} \cos(\omega t)\hat{\mathbf{x}}$ with frequency $\omega = \omega_{\mathrm{gap}}$, and a single skyrmion as an initial state. Figure 2(d) presents snapshots

of the time evolution of magnetization deviation $\mathcal{D}S_x(t) = S_x(t=0) - S_x(t)$ using $h_{ac} = 0.1$, showing that the ac field not only excites the CCW gyration of the skyrmion core but also induces crystal-like long-range localization patterns. The full-time evolution is shown in Movie S1 of the SM [32]. In this case, the magnetically active skyrmion mode provides the coupling to the uniform drive, while the characteristic Mexican-hat magnon dispersion sets the superlattice wavelength. The crystal patterns are absent when starting from an FM state under a spatially uniform ac drive, although a local ac field whose width is comparable to the low-energy magnon wavelength generates the same characteristic pattern without a skyrmion, as demonstrated in Fig. S8 and discussed in Appendix F of SM [32]. They are also absent in the DMI-skyrmion comparison, where the relevant extended magnons are long-wavelength relative to the skyrmion size, suppressing the finite-wavelength interference mechanism (see Fig. S4 in Appendix D of SM [32]).

The patterns are richer at higher energies since they contain both short- and long-wavelength components. Figures 2(e) and 2(f) show the higher-energy CCW2 mode, which forms magnon crystals with shorter periodicities due to interference of shorter-wavelength magnons. The higher-energy CCW3 mode has the largest magnetic moment $\mathcal{M}_x$ and is hybridized with modes at the Γ point and symmetric localization patterns [Figs. 2(i) and 2(j)]. Thus, the interference conditions modify the patterns and lead to regimes of tunable, dynamic magnon localization patterns. We confirm that these structures are observable via LLG simulations [Fig. 2(h) and Movie S2 of SM [32] using $h_{ac} = 0.01$ and $\omega = 0.18$ for the CCW2 mode, and Fig. 2(l) and Movie S3 of SM [32] using $h_{ac} = 0.001$ and $\omega = 0.52$ for CCW3]. In contrast to DMI skyrmions, there is no breathing mode with finite $\mathcal{M}_z$, due to the S_z-conserving $U(1)$ symmetry of the model. Focusing on the lowest breathing mode with $\omega_{BM} \approx \omega_{gap}$, as shown in Figs. 2(m) and 2(n), we conclude that the out-of-plane dipole moment of the skyrmion core $\sum_{i<\lambda} \mathcal{M}_z^i$ cancels out by the opposite dipole moment of the tail, $\sum_{i>\lambda} \mathcal{M}_z^i$, shown in Fig. S2 of SM [32].

To verify that the interference mechanism is not an artifact of perfect rotational symmetry, we performed additional simulations including rotational-symmetry-breaking terms such as dipole-dipole interactions and weak DMI exchange. As shown in Fig. S5 in Appendix D of SM [32], the characteristic real-space modulations remain intact. The magnon superlattices persist with only minor amplitude distortions and unchanged periodicity. This confirms that their wavelength is set primarily by the finite-k_{min} structure of the frustrated-magnet dispersion, while magnon-skyrmion hybridization selects a definite superposition of the degenerate finite-k_{min} states and renders it active under a spatially uniform magnetic drive.

B. Experimental feasibility and detection requirements

The dynamical magnon superlattices predicted here manifest as spatially modulated interference patterns whose periodicity is set by the characteristic magnon wavelength l_{min}, comparable to the skyrmion diameter λ. Prime material platforms are centrosymmetric frustrated magnets in which $\lambda \sim l_{min}$. Notable examples include Gd_2PdSi_3 [44], $Gd_3Ru_4Al_{12}$ [45], and $GdRu_2Si_2$ [46], which host nanometric skyrmion lattices with periods in the few-nanometer range, as well as kagome magnets such as Fe_3Sn_2 [47], where skyrmionic textures are stabilized at room temperature. Their small skyrmion size ensures strong magnon-skyrmion hybridization, while the availability of bulk single crystals and thin films makes them compatible with high-resolution techniques. These compounds should be viewed as candidate material classes rather than ideal realizations of the minimal two-dimensional Hamiltonian of Eq. (1). Metallic or multilayered systems can still display the required frustrated-skyrmion length scales, but electronic damping may broaden the magnon resonances and make spatially resolved detection more demanding.

Energies and frequencies are reported in units of $J_1 S$, while magnetic fields are reported in units of $J_1/(g\mu_B)$. In realistic units of $J_1 = 2\,\text{meV}$, $J_2 = 1\,\text{meV}$, $K = 0.3\,\text{meV}$, $B = hJ_1/(g\mu_B) = 3.9\,\text{T}$, and $a = 0.5\,\text{nm}$, the magnon gap energy appears at $\omega_{gap} = 0.05\,\text{meV}$ (12 GHz), while the skyrmion core is $\lambda = 6\,\text{nm}$. The linewidth of a mode of frequency ω is controlled by damping, $\Delta\omega \sim \alpha\omega$. In the LLG simulations, we use $\alpha = 0.01$, for which the expected linewidth is of order 0.1–0.2 GHz for frequencies in the 10–20 GHz range, smaller than the typical separations between the magnetically active modes. Larger damping, especially in metallic samples, broadens the resonances and reduces the contrast of the superlattice pattern. Resolving these patterns requires imaging techniques with spatial resolution of a few nanometers, achievable with spin-polarized scanning tunneling microscopy (STM) [48,49], magnetic exchange force microscopy (MExFM) [49], scanning transmission x-ray microscopy [50], or nitrogen-vacancy (NV) center magnetometry with a demonstrated NV-to-sample distance around 8 nm [51].

In reciprocal space, the CCW modes occur at frequencies 5%–30% above the magnon gap (10–20 GHz), corresponding to absolute separations of roughly 1–10 GHz for realistic exchange parameters. Although in-plane ac fields can selectively excite CCW modes, their frequencies are close enough that resolving them individually, and thus identifying the corresponding interference patterns, requires subgigahertz spectroscopic resolution. Such performance is well within the reach of Brillouin light scattering [52], time-resolved magneto-optical Kerr effect [53], and x-ray ferromagnetic resonance [54]. Importantly, the predicted interference patterns are robust and persist far from the skyrmion core, allowing detection in both real-space and momentum-resolved measurements. Their weak dependence on system size and the persistence of the characteristic periodicity up to $L = 900$ are demonstrated in Figs. S6 and S7 and discussed in Appendix E of SM [32].

A transverse spin deviation $\mathcal{D}S_x/S = 0.3$ produces a transverse field at the surface $\Delta B_\perp = \mu_0 M_s \mathcal{D}S_x/S = 0.38\,\text{T}$, where we used $M_s = 10^6$ A/m. The field decays exponentially with distance from the surface, giving estimated amplitudes of 40 mT at 10 nm from the surface. Such periodic stray-field modulations are detectable with spin-polarized STM and MExFM techniques, which can directly image the in-plane spin contrast at the surface. Systematic spectroscopic and imaging studies in these materials can directly access the interference-driven localization patterns predicted here.

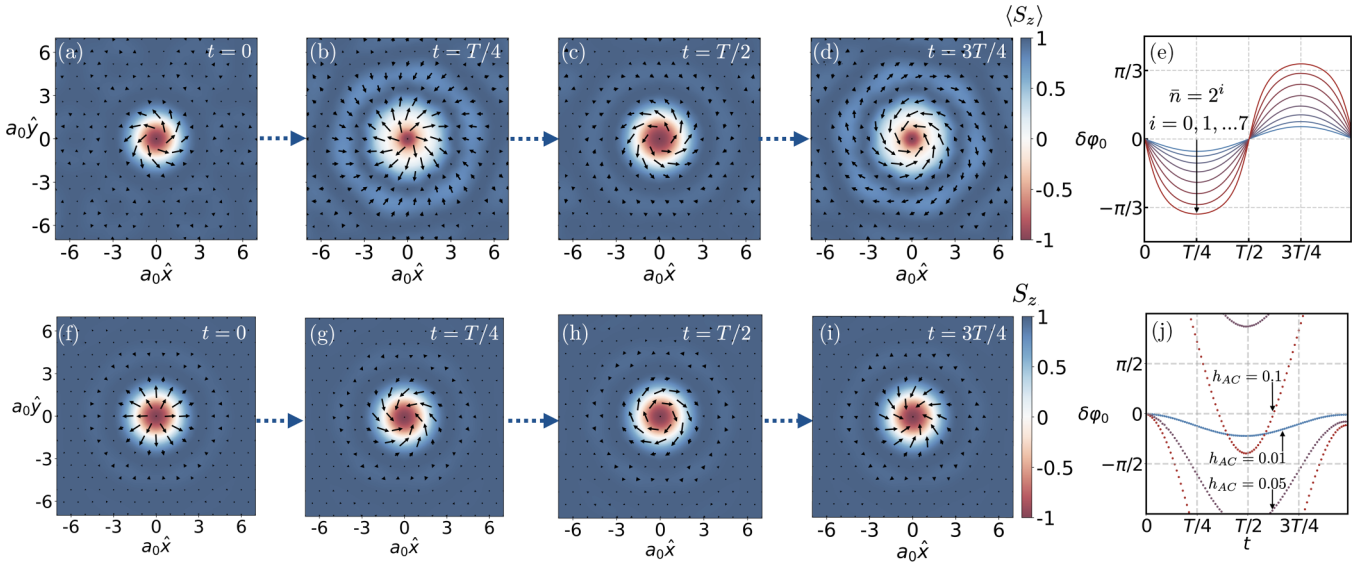


FIG. 3. Helicity-induced nonlinear dynamics. (a)–(d) Isolated skyrmion breathing mode from Figs. 2(m)–2(p) involving coupled oscillation of skyrmion z magnetization and helicity, φ_0, found at $\omega = 0.028$. The average magnon number per lattice site is $\bar{n}/N^2 = 2^7/42^2 \approx 0.073$. Snapshots are taken at equally spaced time steps and cover one full oscillation period. (e) Nonlinear dependence of helicity oscillations over one period on the magnon number $\bar{n}$. (f)–(i) Snapshots of the same breathing mode activated by an out-of-plane magnetic field $h_{\rm ac} = 0.1$ through damping-mediated coupling. (j) Dependence of the helicity oscillation amplitude on the drive amplitude.

Experimental [44] and first-principles studies [55] of Gd-based skyrmion-hosting materials demonstrated that $J_{1,2} \gg J_\perp$, with $J_\perp$ the interlayer coupling, leading to magnetically quasi-two-dimensional behavior. A weak $J_\perp$ does not modify the in-plane finite-k structure or the interference mechanism that gives rise to the magnon superlattices.

C. Collective helicity precession modes

In frustrated magnets, magnon excitations hybridize with the helicity zero mode, with the strongest effects observed for the breathing modes. In Figs. 3(a)–3(d), we depict snapshots of the time evolution of the out-of-plane magnetization $\langle S^z_{\mathbf{n},i}\rangle$ associated with the breathing mode at $\omega = 0.028$. In Fig. 3(e), we plot dynamical deviations of the skyrmion helicity $\delta\varphi_0(t) = \varphi_0(t) - \varphi_0(t=0)$, defined as

$$\varphi_0(t) = \arg\left(\sum_i \sqrt{1 - S^z_i(t)}\sqrt{1 - S^z_{i,0}}\, e^{i(\Phi_i(t) - \Phi_{i,0})}\right), \quad (2)$$

where $\Phi_i = \operatorname{arccot}(S^x_i/S^y_i)$, and $S^z_{i,0}$, $\Phi_{i,0}$ the spin configuration of the initial static skyrmion. The extent of helicity precession depends on the magnon number and saturates at sufficiently large $\bar{n}_i$. In Figs. 3(f)–3(i), we show snapshots of $\mathcal{D}S^z_i(t)$ obtained by solving the LLG equation under an ac drive of amplitude $h_{\rm ac} = 0.1$ and $\omega = 0.028$. We observe a similar oscillation of the skyrmion helicity [Fig. 3(j)], with an amplitude that increases with $h_{\rm ac}$.

The vanishing $\mathcal{M}_z$ for all breathing modes implies that an out-of-plane ac field cannot directly activate them. Nevertheless, numerical simulations of the LLG equation under an ac field $\mathbf{H}_{\rm ac} = h_{\rm ac}\cos(\omega_{\rm BM}t)\hat{\mathbf{z}}$ reveal that the breathing mode is weakly excited [Fig. 2(p)] through an indirect coupling mechanism. Here, the ac field couples to the total skyrmion spin $\mathcal{S}^z_0 = \sum_i (S - S^z_{i,0})$ and activates the oscillation of the skyrmion helicity $\varphi_0(t)$, depicted in Fig. 3(j). In the conservative limit, this motion remains decoupled from the breathing coordinate. Gilbert damping relaxes this constraint and generates a longitudinal spin response, enabling the helicity motion to activate the breathing dynamics. The resulting breathing amplitude is linear in both $h_{\rm ac}$ and α in the weak-drive and weak-damping regime, while its frequency dependence reflects the contribution of several hybridized magnon modes. A detailed discussion is provided in Appendix C of SM [32].

Taken together, these results establish the basis for understanding magnon behavior in the vicinity of a single skyrmion. The following sections on topological magnon bands and coupled-skyrmion dynamics complete this picture by illustrating how these behaviors evolve from isolated textures to periodic or interacting assemblies.

IV. TOPOLOGICAL MAGNON BANDS

A. Skyrmion-lattice magnon band structure

The periodicity of the 2D hexagonal skyrmion crystal gives rise to a magnon band structure with a corresponding hexagonal Brillouin zone. Magnon bands in skyrmion lattices are well established in chiral DMI magnets, where the periodic texture generates collective modes, band gaps, and edge excitations [12]. Here, we compute the magnon bands of a frustrated skyrmion lattice stabilized by competing exchange interactions. Figure 4 shows the lowest-energy magnon bands along the Γ-M-K high-symmetry path. All bands are dispersive due to strong interactions between neighboring skyrmions, particularly the overlap of their tails. Since the skyrmion crystal breaks both translational symmetry and global spin rotational symmetry along the magnetic field axis, two Goldstone modes are expected at the Γ point, where the

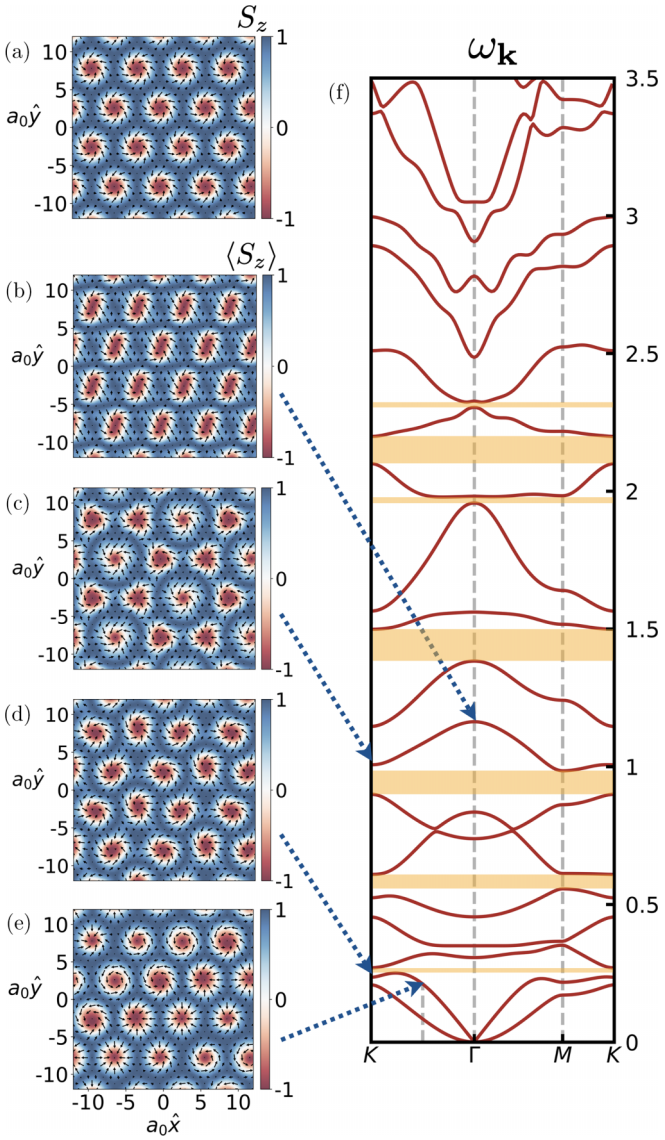


FIG. 4. Magnon bands around skyrmion lattice. (a) Skyrmion lattice ground state at parameters: $J_1 = 1, J_2 = 0.5, h = 0.15/S$, and $K = 0.15$. (b)–(e) Snapshots of excited skyrmions calculated with $\bar{n}_{\mu,\mathbf{k}} = 3$ magnons per unit cell. The symmetry of multipolar modes is dependent on magnon momentum [panels (b) and (c)]. A new band corresponding to helicity excitations emerges and hybridizes with multipolar channels at large $\mathbf{k}$ [panels (d) and (e)]. (f) Magnon band structure of the skyrmion lattice. Band gaps are highlighted in gold, with edges corresponding to frequencies of topologically protected edge states (see Fig. 5). Due to complex skyrmion-skyrmion interactions, multipolar bands are also dispersive in frustrated magnets.

two lowest bands touch zero energy. Due to the discreteness of the spin lattice, a small finite gap appears at $\mathbf{k} = 0$. In addition, a new band emerges above the lowest translational mode, corresponding to precessional dynamics of the skyrmion helicity around its equilibrium value [see Fig. 4(b)].

Within the dispersive multipolar bands, we observe symmetry changes across the Brillouin zone. For example, as shown in Fig. 4(b), a mode exhibiting twofold rotational symmetry at the Γ point transitions to a threefold rotational symmetry at the K point. Similarly, at the edges of the Brillouin zone, the helicity band corresponds to elliptical skyrmion deformations with no change in helicity. Notably, chiral skyrmion lattices support several flat bands associated with nondispersive, localized skyrmion distortions [16]. These flat bands arise due to suppression of skyrmion-skyrmion interactions in the small-skyrmion limit. In contrast, frustrated skyrmions exhibit fluctuating tails that mediate long-range skyrmion-skyrmion interactions [8], leading to a qualitatively different band structure.

We note that each band m can be classified by the following Berry curvature:

$$\mathcal{B}_m(\mathbf{k}) = i\epsilon_{\mu\nu}\mathrm{Tr}[P_m(\mathbf{k})[\partial_{k_\mu}P_m(\mathbf{k})]\partial_{k_\nu}P_m(\mathbf{k})], \tag{3}$$

with $P_m = \mathcal{T}_k\Pi_m\sigma_z\mathcal{T}_k^\dagger\sigma_z$ a projection operator, $(\Pi_m)_{ij} = \delta_{mi}\delta_{ij}$, and $\mathcal{T}_k$ the paraunitary Bogoliubov transformation that diagonalizes the spin-wave Hamiltonian. The corresponding topological Chern index is defined as an integral over the first Brillouin zone $\mathcal{C}_m = \int d\mathbf{k}\mathcal{B}_m(\mathbf{k})/2\pi$ [56]. Topological magnon bands characterized by finite Chern numbers and associated chiral edge modes have emerged as a central theme in magnonics [56]. A particularly rich platform for such phenomena is the skyrmion lattice pattern [57], which supports unidirectional magnon edge states robust against disorder [16]. Nevertheless, intrinsic magnon interactions can compromise the topological protection, leading to the breakdown of chiral edge magnons [58]. Here, we find a number of bands with nonvanishing Chern number presented in Fig. 5. In particular, we note that the low-lying band of helicity excitations is characterized by $\mathcal{C} = 2$ and is accompanied by a global gap, an aspect that is absent in chiral skyrmion lattices. Note that the sign of the Chern number is dictated by the skyrmion's topological charge. In particular, we find that magnon bands in antiskyrmion lattices exhibit Chern numbers of opposite sign, indicating that the band topology can be engineered by tuning the underlying skyrmion topology.

B. Coupled dynamics of interacting skyrmions

Long-range interactions between skyrmions suggest the presence of coupled dynamics in systems of multiple skyrmions. To study this, we stabilized a system of two skyrmions, each with helicity φ_i spaced at a distance $R = |\mathbf{R}|$, illustrated in Figs. 6(a) and 6(f). The pairwise skyrmion interaction depends on separation and skyrmion helicity as $E_{\mathrm{int}} \sim \mathrm{Re}[e^{-qR}]\cos(\varphi_1 - \varphi_2)$, with q a complex number that depends on the model parameters [9], implying that the relative skyrmion helicity $\varphi = \varphi_1 - \varphi_2$ varies with $\mathbf{R}$. For the parameters considered here, we numerically find $\varphi = 0$ when $R = 3n$, with n an even integer, and $\varphi = \pi$, with n an odd integer. The helicity precession is shown in Figs. 6(b)–6(d) for $R = 12$ and Figs. 6(g)–6(i) for $R = 15$. In the former case, we observe a joint precession of skyrmion helicity in opposite directions, while in the latter the two skyrmions precess along the same direction. Notably, similar to Fig. 3, the helicity excitations depend on the total magnon number $\bar{n}$. Figure 6(e) depicts the dependence of the energy of helicity excitation in the coupled system E_φ as a function of separation R for three values of the external magnetic field h. As the distance R grows, the skyrmion interaction diminishes and helicity becomes a zero mode.

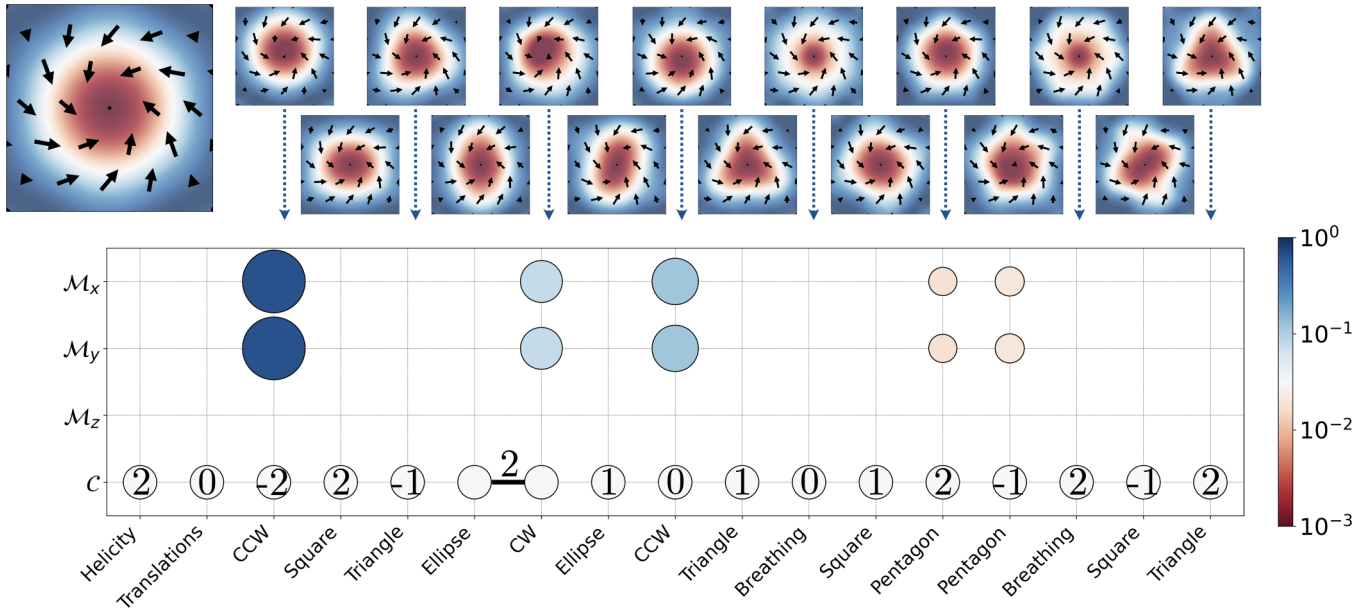


FIG. 5. Topological magnon bands. Magnetic dipole moment $\boldsymbol{\mathcal{M}}_\mu$ and topological Chern numbers $\mathcal{C}$ of the lowest magnon bands shown in Fig. 4. For antiskyrmion lattices, the sign of $\mathcal{C}$ flips, illustrating the dependence of edge state chirality on bulk topology. The neighboring elliptical and CCW bands touch and have a total Chern number of 2. Some topological edge states are observable via in-plane ac magnetic field excitation due to their finite magnetic dipole moment.

V. CONCLUSIONS

We studied dynamic magnonic patterns through geometric and topological engineering in frustrated magnets hosting atomic-scale size magnetic skyrmions possessing helicity as an internal degree of freedom. Our calculations of the magnon spectrum around isolated skyrmions, skyrmion lattices, and interacting skyrmions revealed that the magnon's wavelength

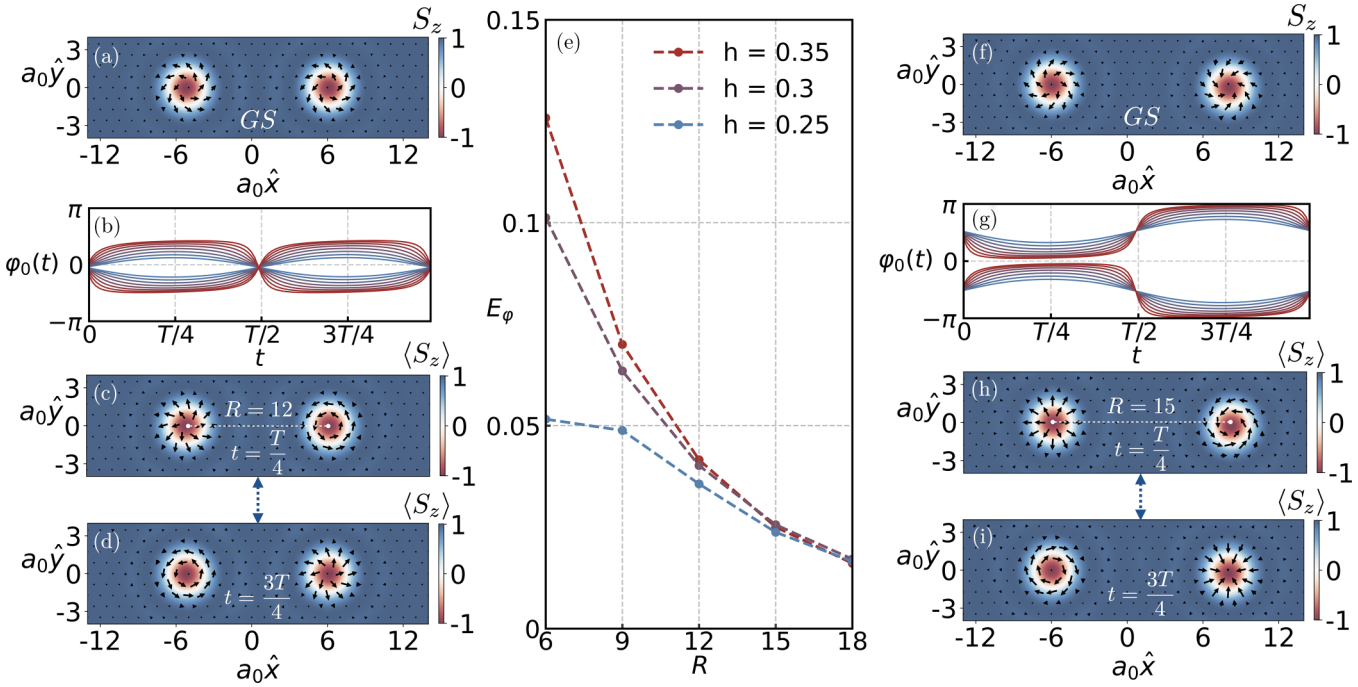


FIG. 6. Helicity excitation of coupled skyrmions. The pairwise skyrmion interaction depends on the separation distance R and the relative skyrmion helicity φ. (a) When $R = 12$, the two skyrmions have the same helicity such that $\varphi = 0$, while in panels (b)–(d), the joint precession of skyrmion helicity occurs in opposite directions. (f) For $R = 15$, the two skyrmions have the opposite helicities such that $\varphi = \pi$, and (g)–(i) helicity precession takes place along the same direction of rotation. Panels (b) and (g) illustrate the dependence of $\varphi_0(t)$ over one period for different magnon numbers $\bar{n}$. Blue to red lines correspond to $\bar{n} = 2^i$, $i = 0, 1, \ldots, 7$.

is comparable to the skyrmion's size. This is distinct from chiral systems where skyrmion-induced effects on extended modes are typically weak due to a large mismatch in length scales. These results indicate strong magnon-skyrmion coupling, leading to emergent dynamical localization phenomena. Specifically, interference between degenerate extended states sets the superlattice periodicity, while hybridization with the skyrmion CCW mode selects and activates the resulting pattern under a spatially uniform ac field.

Furthermore, we demonstrate that helicity acts as an internal dynamical degree of freedom, giving rise to nonlinear behavior such as helicity precession and mode hybridization. Although the model is S_z-conserving, magnetically inactive breathing modes are weakly excited through damping-mediated coupling between the driven helicity and breathing dynamics. In skyrmion lattices, skyrmion interactions give rise to complex dispersive magnon bands with nontrivial Chern numbers within the first bulk gap, confirming the topological nature of the excitations. We also uncover helicity-sensitive coupling between skyrmions, which gives rise to collective dynamics dependent on interskyrmion separation.

Our results reveal a previously unexplored regime of magnon physics, where frustration, topology, and internal skyrmion degrees of freedom coordinate to produce confined and topologically nontrivial spin excitations. These findings deepen the fundamental understanding of magnon behavior in complex spin textures and establish frustrated magnets as a fertile platform for studying emergent quasiparticles and their interactions. These results connect frustrated-skyrmion physics to the broader program of interference-based magnonics. While existing reconfigurable magnonic devices control spin-wave interference through device geometry [25] or externally tuned dispersion [26], the mechanism identified here uses a nanoscale topological texture as an intrinsic mode-selecting element. A single skyrmion can convert finite-wavelength magnon interference into a magnetically active pattern extending far beyond the skyrmion core, suggesting a route toward texture-controlled spin-wave patterning and nanoscale magnon modulation [59,60]. High-energy techniques, imaging, and reconstruction algorithms are now critical to studying and visualizing the dynamical, crystal-like localization patterns we report. A complementary approach will be required, including high-frequency magneto-optics, x-ray ferromagnetic resonance, time-resolved momentum microscopy, and inelastic neutron scattering.

ACKNOWLEDGMENTS

C.P. is an École Normale Supérieure (ENS)-Mitsubishi Heavy Industries (MHI) Chair of Quantum Information supported by MHI. The work in Singapore was supported by the Singapore Ministry of Education (MOE) Academic Research Fund Tier 3 Grant No. MOE-MOET32023-0003.

DATA AVAILABILITY

The data that support the findings of this article are not publicly available upon publication because it is not technically feasible and/or the cost of preparing, depositing, and hosting the data would be prohibitive within the terms of this research project. The data are available from the authors upon reasonable request.

[1] E. Dagotto, Complexity in strongly correlated electronic systems, Science **309**, 257 (2005).

[2] J. Chakhalian, J. W. Freeland, A. J. Millis, C. Panagopoulos, and J. M. Rondinelli, *Colloquium*: Emergent properties in plane view: Strong correlations at oxide interfaces, Rev. Mod. Phys. **86**, 1189 (2014).

[3] Y. Tokura and N. Nagaosa, Nonreciprocal responses from non-centrosymmetric quantum materials, Nat. Commun. **9**, 3740 (2018).

[4] Y. Cao, V. Fatemi, S. Fang, K. Watanabe, T. Taniguchi, E. Kaxiras, and P. Jarillo-Herrero, Unconventional superconductivity in magic-angle graphene superlattices, Nature (London) **556**, 43 (2018).

[5] L. Balents, C. R. Dean, D. K. Efetov, and A. F. Young, Superconductivity and strong correlations in moiré flat bands, Nat. Phys. **16**, 725 (2020).

[6] A. Fert, N. Reyren, and V. Cros, Magnetic skyrmions: Advances in physics and potential applications, Nat. Rev. Mater. **2**, 17031 (2017).

[7] A. P. Petrović, C. Psaroudaki, P. Fischer, M. Garst, and C. Panagopoulos, Colloquium: Quantum properties and functionalities of magnetic skyrmions Rev. Mod. Phys. **97**, 031001 (2025).

[8] A. O. Leonov and M. Mostovoy, Multiply periodic states and isolated skyrmions in an anisotropic frustrated magnet, Nat. Commun. **6**, 8275 (2015).

[9] S.-Z. Lin and S. Hayami, Ginzburg-Landau theory for skyrmions in inversion-symmetric magnets with competing interactions, Phys. Rev. B **93**, 064430 (2016).

[10] C. Psaroudaki and C. Panagopoulos, Skyrmion qubits: A new class of quantum logic elements based on nanoscale magnetization, Phys. Rev. Lett. **127**, 067201 (2021).

[11] C. Psaroudaki and C. Panagopoulos, Skyrmion helicity: Quantization and quantum tunneling effects, Phys. Rev. B **106**, 104422 (2022).

[12] M. Garst, J. Waizner, and D. Grundler, Collective spin excitations of helices and magnetic skyrmions: Review and perspectives of magnonics in non-centrosymmetric magnets, J. Phys. D **50**, 293002 (2017).

[13] C. Schütte and M. Garst, Magnon-skyrmion scattering in chiral magnets, Phys. Rev. B **90**, 094423 (2014).

[14] M. Mochizuki, X. Z. Yu, S. Seki, N. Kanazawa, W. Koshibae, J. Zang, M. Mostovoy, Y. Tokura, and N. Nagaosa, Thermally driven ratchet motion of a skyrmion microcrystal and topological magnon Hall effect, Nat. Mater. **13**, 241 (2014).

[15] Z. Jin, C. Y. Meng, T. T. Liu, D. Y. Chen, Z. Fan, M. Zeng, X. B. Lu, X. S. Gao, M. H. Qin, and J.-M. Liu, Magnon-driven skyrmion dynamics in antiferromagnets: Effect of magnon polarization, Phys. Rev. B **104**, 054419 (2021).

[16] S. A. Díaz, T. Hirosawa, J. Klinovaja, and D. Loss, Chiral magnonic edge states in ferromagnetic skyrmion crystals controlled by magnetic fields, Phys. Rev. Res. **2**, 013231 (2020).

[17] T. Weber, D. M. Fobes, J. Waizner, P. Steffens, G. S. Tucker, M. Böhm, L. Beddrich, C. Franz, H. Gabold, R. Bewley, D. Voneshen, M. Skoulatos, R. Georgii, G. Ehlers, A. Bauer, C. Pfleiderer, P. Böni, M. Janoschek, and M. Garst, Topological magnon band structure of emergent Landau levels in a skyrmion lattice, Science **375**, 1025 (2022).

[18] S. Seki, M. Garst, J. Waizner, R. Takagi, N. D. Khanh, Y. Okamura, K. Kondou, F. Kagawa, Y. Otani, and Y. Tokura, Propagation dynamics of spin excitations along skyrmion strings, Nat. Commun. **11**, 256 (2020).

[19] P. Y. Portnichenko, J. Romhányi, Y. A. Onykiienko, A. Henschel, M. Schmidt, A. S. Cameron, M. A. Surmach, J. A. Lim, J. T. Park, A. Schneidewind, D. L. Abernathy, H. Rosner, J. van den Brink, and D. S. Inosov, Magnon spectrum of the helimagnetic insulator Cu_2OSeO_3, Nat. Commun. **7**, 10725 (2016).

[20] P. Che, R. Ciola, M. Garst, V. Kravchuk, P. R. Baral, A. Magrez, H. Berger, T. Schönenberger, H. M. Rønnow, and D. Grundler, Multipole magnons in topological skyrmion lattices resolved by cryogenic Brillouin light scattering microscopy Commun. Mater. **6**, 139 (2024).

[21] S. A. Montoya, S. Couture, J. J. Chess, J. C. T. Lee, N. Kent, M.-Y. Im, S. D. Kevan, P. Fischer, B. J. McMorran, S. Roy, V. Lomakin, and E. E. Fullerton, Resonant properties of dipole skyrmions in amorphous Fe/Gd multilayers, Phys. Rev. B **95**, 224405 (2017).

[22] B. Satywali, V. P. Kravchuk, L. Pan, M. Raju, S. He, F. Ma, A. P. Petrović, M. Garst, and C. Panagopoulos, Microwave resonances of magnetic skyrmions in thin film multilayers, Nat. Commun. **12**, 1909 (2021).

[23] G. Talmelli, T. Devolder, N. Träger, J. Förster, S. Wintz, M. Weigand, H. Stoll, M. Heyns, G. Schütz, I. P. Radu, J. Gräfe, F. Ciubotaru, and C. Adelmann, Reconfigurable submicrometer spin-wave majority gate with electrical transducers, Sci. Adv. **6**, eabb4042 (2020).

[24] A. V. Chumak, A. A. Serga, and B. Hillebrands, Magnon transistor for all-magnon data processing, Nat. Commun. **5**, 4700 (2014).

[25] Q. Wang, P. Pirro, R. Verba, A. Slavin, B. Hillebrands, and A. V. Chumak, Reconfigurable nanoscale spin-wave directional coupler, Sci. Adv. **4**, e1701517 (2018).

[26] M. S. Sarker, L. Yao, H. Yamahara, K. Ma, Z. Liao, K. Terao, S. Tang, S. G. Ramaraj, M. Seki, and H. Tabata, Reconfigurable magnon interference by on-chip dynamic wavelength conversion, Sci. Rep. **13**, 4872 (2023).

[27] S. Hayami, S.-Z. Lin, and C. D. Batista, Bubble and skyrmion crystals in frustrated magnets with easy-axis anisotropy, Phys. Rev. B **93**, 184413 (2016).

[28] N. Metropolis and S. Ulam, The Monte Carlo method, J. Am. Stat. Assoc. **44**, 335 (1949).

[29] T. Holstein and H. Primakoff, Field dependence of the intrinsic domain magnetization of a ferromagnet, Phys. Rev. **58**, 1098 (1940).

[30] J. Colpa, Diagonalization of the quadratic boson Hamiltonian, Physica A **93**, 327 (1978).

[31] S. Toth and B. Lake, Linear spin wave theory for single-q incommensurate magnetic structures, J. Phys.: Condens. Matter **27**, 166002 (2015).

[32] See Supplemental Material at http://link.aps.org/supplemental/10.1103/fhbj-ykvn for detailed derivations, theoretical analysis, and additional numerical simulations.

[33] G. Tatara, H. Kohno, and J. Shibata, Microscopic approach to current-driven domain wall dynamics, Phys. Rep. **468**, 213 (2008).

[34] Y. V. Tymoshenko, Y. A. Onykiienko, T. Müller, R. Thomale, S. Rachel, A. S. Cameron, P. Y. Portnichenko, D. V. Efremov, V. Tsurkan, D. L. Abernathy, J. Ollivier, A. Schneidewind, A. Piovano, V. Felea, A. Loidl, and D. S. Inosov, Pseudo-Goldstone magnons in the frustrated $S = 3/2$ Heisenberg helimagnet $ZnCr_2Se_4$ with a pyrochlore magnetic sublattice, Phys. Rev. X **7**, 041049 (2017).

[35] M. Speight and T. Winyard, Skyrmions and spin waves in frustrated ferromagnets at low applied magnetic field, Phys. Rev. B **101**, 134420 (2020).

[36] M. Kataoka, Spin waves in the helical spin density wave state due to the antisymmetric exchange interaction, J. Magn. Magn. Mater. **31–34**, 341 (1983).

[37] G. M. Wysin and A. R. Völkel, Normal modes of vortices in easy-plane ferromagnets, Phys. Rev. B **52**, 7412 (1995).

[38] S.-Z. Lin, C. D. Batista, and A. Saxena, Internal modes of a skyrmion in the ferromagnetic state of chiral magnets, Phys. Rev. B **89**, 024415 (2014).

[39] T. Hirosawa, A. Mook, J. Klinovaja, and D. Loss, Magnetoelectric cavity magnonics in skyrmion crystals, PRX Quantum **3**, 040321 (2022).

[40] M. Mochizuki, Spin-wave modes and their intense excitation effects in skyrmion crystals, Phys. Rev. Lett. **108**, 017601 (2012).

[41] Y. Onose, Y. Okamura, S. Seki, S. Ishiwata, and Y. Tokura, Observation of magnetic excitations of skyrmion crystal in a helimagnetic insulator Cu_2OSeO_3, Phys. Rev. Lett. **109**, 037603 (2012).

[42] S. A. Díaz, T. Hirosawa, D. Loss, and C. Psaroudaki, Spin wave radiation by a topological charge dipole, Nano Lett. **20**, 6556 (2020).

[43] N. Zagury and S. M. Rezende, Theory of macroscopic excitations of magnons, Phys. Rev. B **4**, 201 (1971).

[44] T. Kurumaji, T. Nakajima, M. Hirschberger, A. Kikkawa, Y. Yamasaki, H. Sagayama, H. Nakao, Y. Taguchi, T.-h. Arima, and Y. Tokura, Skyrmion lattice with a giant topological Hall effect in a frustrated triangular-lattice magnet, Science **365**, 914 (2019).

[45] M. Hirschberger, T. Nakajima, S. Gao, L. Peng, A. Kikkawa, T. Kurumaji, M. Kriener, Y. Yamasaki, H. Sagayama, H. Nakao, K. Ohishi, K. Kakurai, Y. Taguchi, X. Yu, T.-H. Arima, and Y. Tokura, Skyrmion phase and competing magnetic orders on a breathing kagomé lattice, Nat. Commun. **10**, 5831 (2019).

[46] N. D. Khanh, T. Nakajima, X. Yu, S. Gao, K. Shibata, M. Hirschberger, Y. Yamasaki, H. Sagayama, H. Nakao, L. Peng, K. Nakajima, R. Takagi, T.-H. Arima, Y. Tokura, and S. Seki, Nanometric square skyrmion lattice in a centrosymmetric tetragonal magnet, Nat. Nanotechnol. **15**, 444 (2020).

[47] Z. Hou, W. Ren, B. Ding, G. Xu, Y. Wang, B. Yang, Q. Zhang, Y. Zhang, E. Liu, F. Xu, W. Wang, G. Wu, X. Zhang, B. Shen, and Z. Zhang, Observation of various and spontaneous magnetic skyrmionic bubbles at room temperature in a frustrated

kagome magnet with uniaxial magnetic anisotropy, Adv. Mater. **29**, 1701144 (2017); Erratum **30**, 1706306 (2018).

[48] A. Kubetzka, M. Bode, O. Pietzsch, and R. Wiesendanger, Spin-polarized scanning tunneling microscopy with antiferromagnetic probe tips, Phys. Rev. Lett. **88**, 057201 (2002).

[49] R. Wiesendanger, Spin mapping at the nanoscale and atomic scale, Rev. Mod. Phys. **81**, 1495 (2009).

[50] T. Mamyrbayev, K. Ikematsu, P. Meyer, A. Ershov, A. Momose, and J. Mohr, Super-resolution scanning transmission X-ray imaging using single biconcave parabolic refractive lens array, Sci. Rep. **9**, 14366 (2019).

[51] Z. Xu, M. L. Palm, W. Huxter, K. Herb, J. M. Abendroth, K. Bouzehouane, O. Boulle, M. S. Gabor, J. Urrestarazu Larranaga, A. Morales, J. Rhensius, G. Puebla-Hellmann, and C. L. Degen, Minimizing sensor-sample distances in scanning nitrogen-vacancy magnetometry, ACS Nano **19**, 8255 (2025).

[52] T. Sebastian, K. Schultheiss, B. Obry, B. Hillebrands, and H. Schultheiss, Micro-focused Brillouin light scattering: Imaging spin waves at the nanoscale, Front. Phys. **3** (2015).

[53] Y. Acremann, J. P. Strachan, V. Chembrolu, S. D. Andrews, T. Tyliszczak, J. A. Katine, M. J. Carey, B. M. Clemens, H. C. Siegmann, and J. Stöhr, Time-resolved imaging of spin transfer switching: Beyond the macrospin concept, Phys. Rev. Lett. **96**, 217202 (2006).

[54] S. Bonetti, M. C. Hoffmann, M.-J. Sher, Z. Chen, S.-H. Yang, M. G. Samant, S. S. P. Parkin, and H. A. Dürr, THz-driven ultrafast spin-lattice scattering in amorphous metallic ferromagnets, Phys. Rev. Lett. **117**, 087205 (2016).

[55] T. Nomoto, T. Koretsune, and R. Arita, Formation mechanism of the helical Q structure in Gd-based skyrmion materials, Phys. Rev. Lett. **125**, 117204 (2020).

[56] R. Shindou, R. Matsumoto, S. Murakami, and J.-I. Ohe, Topological chiral magnonic edge mode in a magnonic crystal, Phys. Rev. B **87**, 174427 (2013).

[57] S. A. Díaz, J. Klinovaja, and D. Loss, Topological magnons and edge states in antiferromagnetic skyrmion crystals, Phys. Rev. Lett. **122**, 187203 (2019).

[58] J. Habel, A. Mook, J. Willsher, and J. Knolle, Breakdown of chiral edge modes in topological magnon insulators, Phys. Rev. B **109**, 024441 (2024).

[59] E. Albisetti, D. Petti, G. Sala, R. Silvani, S. Tacchi, S. Finizio, S. Wintz, A. Calò, X. Zheng, J. Raabe, E. Riedo, and R. Bertacco, Nanoscale spin-wave circuits based on engineered reconfigurable spin-textures, Commun. Phys. **1**, 56 (2018).

[60] H. Yu, J. Xiao, and H. Schultheiss, Magnetic texture based magnonics, Phys. Rep. **905**, 1 (2021).